# Performance Improvement in Polymer/ZnO Nanoarray Hybrid Solar Cells by Formation of ZnO/CdS-Core/Shell Heterostructures

Qi Cui, Changwen Liu, Fan Wu, Wenjin Yue, Zeliang Qiu, Hui Zhang, Feng Gao, Wei Shen, and Mingtai Wang*

Institute of Plasma Physics and Key Laboratory of Novel Thin Film Solar Cells, Chinese Academy of Sciences, Hefei 230031, P. R. China

S *Supporting Information*

ABSTRACT: In this paper, performance in hybrid solar cells based on ZnO nanorod array (ZnO-NA) is significantly improved by formation of a heterostructured ZnO/CdS-core/shell nanorod array (ZnO-CdS-NA), the CdS shell effects on device performance including charge transport and recombination dynamics are discussed, and a model concerning ineffective polymer phase is proposed for understanding the charge generation upon CdS shell formation. The ZnO-CdS-NAs with varied CdS shell thickness (L) were prepared by depositing CdS quantum dots on the ZnO nanorods in the ZnO-NA. Solar cells were prepared by filling the interspaces between the nanorods in ZnO-NA or ZnO-CdS-NAs with poly(2-methoxy-5-(2-ethylhexyloxy)-1,4-phenylenevinylene) (MEH-PPV). Compared to MEH-PPV/ZnO-NA devices, both open-circuit voltage (V_{oc}) and short-circuit current (J_{sc}) in MEH-PPV/ZnO-CdS-NA solar cells were dramatically improved depending on L, resulting in a peak efficiency of ca. 1.23% under AM 1.5 illumination (100 mW/cm^2) with a 7-fold increment for L = 6 nm. In particular, the experimental L-dependence of J_{sc} agreed with the expectation from the proposed model and the V_{oc} was improved from ca. 0.4 V for ZnO-NA up to around 0.8 V. Results demonstrate that in the MEH-PPV/ZnO-CdS-NA devices, the J_{sc} correlates mainly with the charge generation subjected to the exciton generation altered by CdS shell formation, in which the polymer absorption is dominantly contributive; however, the V_{oc} is determined by the energy difference between the highest occupied molecular orbital level of MEH-PPV and the conduction band edge of ZnO but significantly correlates with the quasi-Fermi levels of the electrons in ZnO nanorods.
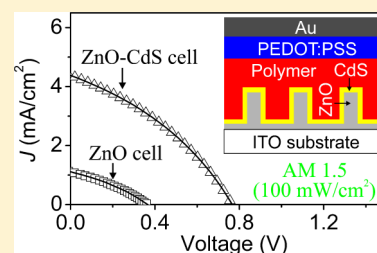
1. INTRODUCTION

Polymer-based solar cells (PSCs) with a photoactive layer consisting of an organic conjugated polymer as electron donor (D) and inorganic nanostructures as electron acceptor (A) in a hybrid bulk-heterojunction (BHJ) structure are promising for low-cost solar cells, due to their particular advantages such as integrating the properties of both organic and inorganic components, lightweight and easy-processability.[1−3] In these hybrid devices, the polymer, poly(3-hexylthiophene) (P3HT) or poly(2-methoxy-5-(2-ethylhexyloxy)-1,4-phenylene vinylene) (MEH-PPV) for example, and nanostructures form the D/A interfaces for exciton dissociation and charge generation. Use of vertically aligned one-dimensional (1D) inorganic nanostructure arrays, instead of the disordered A-phase pathways in the simple blends of polymer and nanoparticles, can provide an ideal architecture for efficient BHJ devices,[1−3] which have the high D/A interface area for exciton dissociation, the straightforward nanochannels for high mobility electron transport with a reduced charge recombination, and the stabilized spatial distribution of D/A interfaces and electron transport pathways for long-term application at evaluated temperatures. Zinc oxide (ZnO) nanorod/nanowire array (ZnO-NA) is the most widely used 1D structure for such aligned BHJ devices (i.e., polymer/ZnO-NA solar cells),[4−6] because of its high electron mobility and easy availability by

many synthesis scenarios. However, the power conversion efficiency (η) of the polymer/ZnO-NA devices is not high yet (η = 0.1−0.5%), most devices exhibit a rather low open-circuit voltage (V_{oc}) of 0.2−0.4 V even though the short-circuit current (J_{sc}) has reached the level of milliamp per centimeter square.

Modification of inorganic nanostructure surfaces with small organic molecules is an efficient strategy to improve the interfacial properties and device performance in their hybrid PSCs.[7−14] Organic modification mainly enhances the compatibility between polymer and ZnO nanorods in the polymer/ZnO-NA devices, resulting in a remarkably improved J_{sc} but still a rather low V_{oc} (<0.4 V).[13−15] Inorganic modification of ZnO nanorod surfaces is another choice for improving the performance of polymer/ZnO-NA solar cells. Greene and Lee[16,17] used titanium dioxide (TiO$_2$) film as shell layer to modify ZnO-NA, resulting in ZnO/TiO$_2$-core/shell nanorod array (ZnO-TiO$_2$-NA). Compared to P3HT/ZnO-NA devices, P3HT/ZnO-TiO$_2$-NA solar cells exhibited a higher J_{sc} with only slightly increased V_{oc} (<0.55 V). Lee et al.[18] coated the ZnO-NA with a thin shell of amorphous titanium oxide (TiO$_x$), producing the increased V_{oc} up to 0.8 V but a greatly decreased

J_{sc} in P3HT/ZnO-TiO$_x$-NA devices because of the TiO$_x$ barrier effect on the charge transfer from the polymer to ZnO. Recently, Wang et al.[19] sensitized ZnO-NA with cadmium sulfide (CdS) quantum dots and achieved the V_{oc} up to 0.85 V, as well as the improved J_{sc} depending on the CdS contents, in the CdS-sensitized MEH-PPV/ZnO-NA devices. Even though those efforts have increased the device performance more or less, the low efficiency ($\eta < 0.7\%$) of the inorganics-modified polymer/ZnO-NA devices needs further improvement for practical application. In particular, understanding the intrinsic correlation between device performance and interfacial property due to inorganic modification is crucially important for the optimized photovoltaic materials and efficient device architectures, on which there is still insufficient knowledge. For example, the improved V_{oc} by the TiO$_x$ shell formation is explained from the decrease in reverse saturation current on the basis of a modified ideal diode equation,[18] and the improved device V_{oc} upon CdS-sensitization is attributed to the band offset between CdS and ZnO in the cascading energy band structure formed upon CdS deposition,[19,20] but it is difficult to account for the dependence of V_{oc} on the CdS volume over ZnO surface from the band-offset standpoint (see later text). In addition, the improved IPCE, and J_{sc} as well, upon the CdS-sensitization are believed to correlate with the cascade band structure formed with the CdS coating that ensures the contributions from the three components (i.e., ZnO, CdS, and MEH-PPV) to photocurrent and the reduced charge recombination for a high charge extraction efficiency.[19]

Heterostructured ZnO/CdS-core/shell nanorod array (ZnO-CdS-NA)[21−24] and ZnO/CdS/P3HT-core/shell three-component nanotube array[25] have been used as photoanodes, in combination with an electrolyte solution, to prepare so-called quantum dot-sensitized solar cells (QDSSCs), suggesting an effective strategy for improving photocurrent in QDSSC devices by application of core−shell heterojunctions. However, there are hitherto no reports on the polymer/ZnO-CdS-NA solar cells. In this paper, we show a facile approach based on formation of ZnO-CdS-NA for significant performance improvement in polymer/ZnO-NA solar cells, and the intrinsic effects of CdS shell therein are revealed. The solar cell architecture in this study is illustrated in Figure 1. To prepare
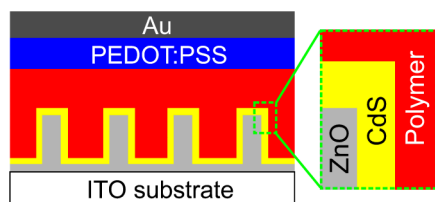

Figure 1. Solar cell architecture. The framed part shows the composition in the device photoactive layer.

the ZnO-CdS-NA, we coated the ZnO nanorods in the ZnO-NA hydrothermally grown on ITO substrate with thin polycrystalline films of CdS quantum dots by successive ion layer adsorption and reaction (SILAR) technique. Compared to MEH-PPV/ZnO-NA devices, MEH-PPV/ZnO-CdS-NA solar cells exhibit much higher J_{sc} and V_{oc}, resulting in a peak efficiency of $\eta = 1.23\%$ that is much higher than the reported efficiencies in CdS-sensitized MEH-PPV/ZnO-NA ($\eta = 0.65\%$)[19] and planar P3HT/CdS/ZnO ($\eta = 0.11\%$)[20] devices.

2. EXPERIMENTAL SECTION

2.1. Synthesis of ZnO-CdS-NA. ZnO-NA was hydrothermally grown on indium tin oxide-coated glass (ITO, ≤15 Ω/□, Shenzhen Laibao Hi-Tech Co., Ltd.) as reported previously.[26] Deposition of CdS on the ZnO-NA was carried out by SILAR technique.[21] Typically, ZnO-NA was first immersed in 10 mM aqueous solution of Cd(NO$_3$)$_2$ for 30 s and rinsed with water, followed by immersion in 10 mM Na$_2$S aqueous solution for 30 s and water rinse, which is referred to as one SILAR cycle. After the ZnO-NA had been subjected to a given SILAR cycle number, the heterostructured ZnO-CdS-NA with a defined CdS shell thickness (L) was obtained, which was dried in nitrogen gas stream and stored in ambient conditions for use.

2.2. Device Fabrication. A layer of MEH-PPV (avg M_n = 40 000−70 000, Aldrich) was deposited on top of ZnO-CdS-NA or ZnO-NA by spin-coating (1500 rpm, 60 s) the polymer solution in chlorobenzene (10 mg/mL) under ambient conditions, followed by annealing at 150 °C for 20 min under a nitrogen atmosphere to get a full infiltration of MEH-PPV into the interspaces between nanorods. Afterward, a film of poly(3,4-ethylenedioxythiophene):poly(styrenesulfonate) (PEDOT:PSS) (Clevios PH500, H. C. Starck) was spin-coated (2000 rpm, 60 s) over the polymer layer, for which the PEDOT:PSS solution with 2-propanol (50% in volume) was filtered with a 0.80 μm filter after an ultrasonic treatment for 15 min prior to use. After the deposition of PEDOT:PSS, the sample was heated for 15 min at 100 °C under a nitrogen atmosphere. Finally, a gold electrode (100 nm in thickness) was thermally evaporated through a shadow mask to form a top contact of 1 × 4 mm^2, which defined the active area of each device. The devices were sealed in a glovebox (O$_2$ < 1 ppm, H$_2$O < 1 ppm) under a N$_2$ atmosphere.

2.3. Characterization. Scanning electron microscopy (SEM) measurements were performed on a field-emission scanning electron microscope (FESEM, FEI-Sirion 200). Transmission electron microscopy (TEM) and high-resolution TEM (HRTEM) studies were done on a JEOL-2010 microscope under an acceleration voltage of 200 kV. X-ray diffraction (XRD) data were collected on Philips X'Pert Pro MPD with Cu Kα radiation ($\lambda = 1.540\,56$ Å). The absorption spectra were obtained by a Shimadzu UV-2550 spectrophotometer and the photoluminescence (PL) spectra by a Hitachi F-7000 spectrofluorophotometer. Both absorption and PL spectra were measured under illumination from the polymer side, and the optical samples were also annealed at 150 °C for 20 min under N$_2$ atmosphere before measurement. Solar cells were characterized with current−voltage ($J−V$) measurements, intensity modulated photocurrent spectroscopy (IMPS) and intensity modulated photovoltage spectroscopy (IMVS), and incident photon-to-current efficiency (IPCE) spectrum. Steady-state $J−V$ curves were measured with AM 1.5 illumination of 100 mW/cm^2 calibrated with a reference solar cell (91150 V, Newport) under ambient conditions on a 94023A Oriel Sol3A solar simulator (Newport) with a 450 W xenon lamp as the light source, and the data were collected with an Oriel I−V test station (PVIV-1A, Keithley 2400 Source Meter, Labview 2009 SP1 GUI Software, Newport). IMPS and IMVS spectra were measured on a controlled intensity modulated photo spectroscopy (CIMPS) (Zahner Co.) in ambient conditions with a background intensity of 15.85 mW/cm^2 as described elsewhere.[26] IPCE spectra were recorded on a QE/IPCE

Measurement Kit (Newport) that was automatically controlled by Oriel Tracq Basic V5.0 software with the light from a 300 W xenon lamp focused through a monochromator (74125 Oriel Cornerstone 260 1/4 m) onto the solar cells under test, where light intensity and photocurrent generated were measured with a 2931-C dual channel power/current meter and a 71675 calibrated UV silicon photodetector.

3. RESULTS AND DISCUSSION

3.1. Heterostructure Characterization. SEM image (Figure 2a) shows that the ZnO nanorods in ZnO-NA are
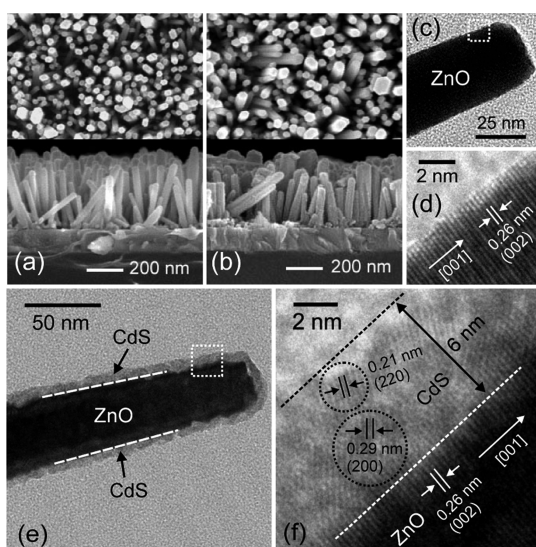

Figure 2. SEM images of ZnO-NA (a) and ZnO-CdS-NA with $L = 6$ nm (b) on ITO substrates. TEM (c, e) and HRTEM (d, f) images of ZnO (c, d) and ZnO/CdS-core/shell (e, f) nanorods, obtained from the samples in (a) and (b), respectively. The HRTEM images were taken from the marked regions on the TEM images, and the cycles in (f) identify individual CdS quantum dots.

vertically aligned on the ITO substrate with a length of ca. 400 nm, a diameter of 20−50 nm, and a number density of about $(4-5) \times 10^2/\mu m^2$, agreeing with previous results;[26] after CdS deposition, the morphology of the original nanorod array is not remarkably altered (Figure 2b). TEM images confirm that the original ZnO nanorod in ZnO-NA (Figure 2c) is turned into a core/shell structure after CdS deposition (Figure 2e). On the HRTEM images (Figure 2d,f), the lattice spacing of 0.26 nm in the core region corresponds to the (002) plane of hexagonal ZnO (JCPDS 36-1451), whereas the lattice fringes of 0.21 and 0.29 nm in the shell layer match respectively the spacing distances of (220) and (200) crystal planes of cubic CdS (JCPDS 80-0019). Clearly, the ZnO nanorods are grown along the [001] direction in agreement with literature,[27] and CdS deposition on ZnO-NA results in ZnO/CdS-core/shell nano-rod array (ZnO-CdS-NA). Careful inspection reveals that the CdS shell is indeed a polycrystalline film consisting of CdS quantum dots with a diameter of 2−4 nm for $L = 6$ nm. In this experiment, the CdS shells with thickness L of 3, 6, and 8 nm were prepared (Figure S1, Supporting Information). HRTEM images (Figures 2f and S1, Supporting Information) showed that the shell film with $L = 3$ nm is actually a monolayer of CdS quantum dots in direct contact with ZnO surface, but those with $L = 6$ and 8 nm are irregularly agglomeration of CdS quantum dots.

Figure 3 compares the XRD patterns of the original ZnO-NA and the ZnO-CdS-NA samples with different L values. The
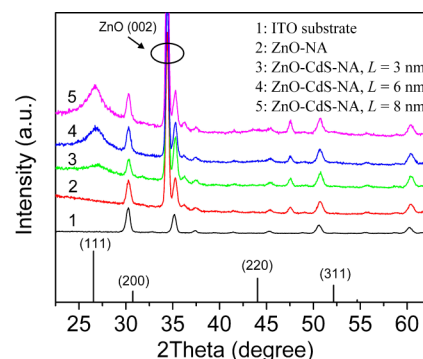

Figure 3. XRD patterns of nanoarray samples. The vertical lines show the XRD pattern of cubic CdS.

XRD data show that the wurtzite ZnO nanorods grow preferentially along the [001] direction, in agreement with the HRTEM data. After CdS deposition, the ZnO-NA samples exhibit the (111) peak of cubic CdS (JCPDS 80-0019) and the (111) peak intensity is enhanced with increasing L. To evaluate the quantum dot size, the (111) peaks of the samples were fitted with a Gaussian shape to get the full width half-maximum (fwhm), where the 2θ value of (111) peak was defined as the center position of the Gaussian fit. The averaged sizes (S) of the nanocrystals in the CdS shells were calculated to be 3.23 nm ($L = 3$ nm), 3.99 nm ($L = 6$ nm), and 4.10 nm ($L = 8$ nm) by Scherrer formula $S = K\lambda(B \cos \theta)^{-1}$, where K is a constant (0.9), λ is the wavelength of the X-ray (1.54056 Å), B is the fwhm (in radians), and θ is the Bragg angle of (111) peak. The XRD results indicate that thicker CdS shell contains larger CdS quantum dots, in agreement with the HRTEM data (Figures 2f and S1, Supporting Information).

Figure 4 shows the absorption and room temperature photoluminescence (PL) spectra of pristine ZnO-NA and different ZnO-CdS-NA samples ($L = 3-8$ nm). ZnO-NA exhibits the band gap absorption edge at 388 nm (Figure 4a). The ZnO-CdS-NA samples show, besides the ZnO absorption, the CdS absorption in a form of shoulder peak in 400−550 nm,[28,29] and the CdS absorption intensity increases with increasing L. The band gap (E_g) of CdS layer in each ZnO-CdS-NA sample was estimated by the direct band gap method to be 2.72, 2.60, and 2.54 eV for $L = 3$, 6, and 8 nm, respectively, agreeing with the previous reports on the ZnO-CdS-NA with a comparable CdS thickness[21] and the synthesized CdS quantum dots with a size 2.8−4.8 nm.[30] Moreover, the measured E_g values agree well with the predicted data (inset to Figure 4a) by the quantum-confinement model,[31] where the effective masses of $m_e^* = 0.18$ for the electron and $m_h^* = 0.53$ for the hole in CdS, $E_g = 2.4$ eV for bulk CdS,[20,28,29] and the averaged CdS crystal sizes detected in XRD measurements were taken for calculation. The E_g larger than the bulk value indicates the remarkable quantum size effect in the CdS shells. As shown in Figure 4b, the pristine ZnO-NA exhibits a near band edge (NBE) emission at 384 nm and a wide peak centered at 555 nm for the deep level emission (DLE). The origin of DLE has been, sometimes controversially, attributed to several intraband defects in crystals, such as oxygen vacancy, zinc vacancy, oxygen interstitial, zinc interstitial, and oxygen antisite, in which at least oxygen and
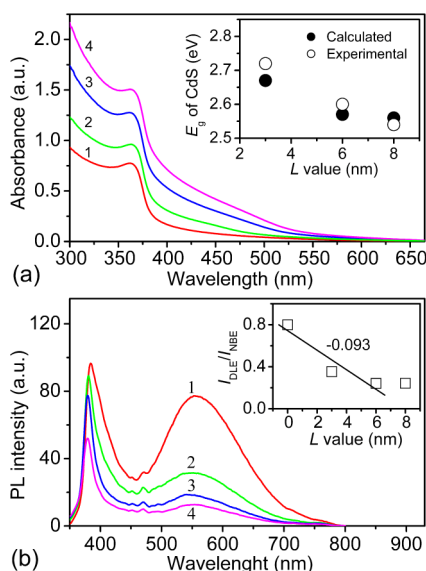
Figure 4. (a) Absorption and (b) room temperature PL (excited at 325 nm) spectra of ZnO-NA (curve 1) and ZnO-CdS-NA with $L = 3$ (curve 2), 6 (curve 3), and 8 (curve 4) nm. The inset to (a) shows the L-dependence of the E_g values of CdS shells (○), compared to the calculated data (●) from the quantum-confinement model; the inset to (b) depicts the L-dependence of I_{DLE}/I_{NBE} ratios, where the line was calculated by linear regression for experimental data expressed by scatters and the numeral marked is the line slope.

zinc vacancies have been generally claimed to contribute to the DLE.[32] The PL spectra of ZnO-CdS-NA samples display emission profiles similar to those of the pristine ZnO-NA in the measured range from 350 to 800 nm, which suggests that the remaining luminescence in the ZnO-CdS-NA samples is due to the radiative decay of the excitons from ZnO. The emissions of CdS nanoparticles[33,34] are not evidently observed in the ZnO-CdS-NA samples, indicating an effective electron transfer from excited CdS shell to ZnO nanorod because of the favorable staggered band alignment between ZnO and CdS[19,20] (also refer to Figure 7a). Upon increasing L from 0 to 6 nm, the DLE peaks are significantly reduced, and the NBE emission and DLE are blue-shifted by ca. 5 nm (NBE emission) and 6 nm (DLE); however, a further increase in L up to 8 nm does not evidently change the positions of the NBE emission and DLE peaks, and the DLE intensity is only reduced weakly.

With deposition of CdS quantum dots, the structural characteristics of ZnO nanorod surface will be changed. During the SILAR process, the Cd^{2+} cations in solution will occupy Zn vacancies,[35] and the S^{2-} anions in solution are easily captured by oxygen vacancies because of the similar chemical properties of oxygen and sulfur atoms.[36] The Cd^{2+} and S^{2-} ions captured by the surface defects of ZnO nanorods provide the initial nucleation for surface growth of CdS quantum dots, which will lead to reduced surface defects on ZnO nanorods with CdS growth.[33,34,36] Therefore, the reduced DLE intensity reasonably correlates with the reduced surface defects originating from oxygen and zinc vacancies. The intensity ratio between the DLE and NBE emission (I_{DLE}/I_{NBE}) is an indication of crystal quality, and a larger ratio of I_{DLE}/I_{NBE} means a higher concentration of surface defects.[32] The I_{DLE}/I_{NBE} ratio decreased almost linearly with increasing L in the range $L = 0$–6 nm (inset to Figure 4b); however, further increasing L from 6 to 8 nm did not change remarkably the I_{DLE}/I_{NBE} ratio.

The L-dependence of I_{DLE}/I_{NBE} ratios, as well as that of emission peak positions, indicates that growth of CdS shell up to $L \approx 6$ nm has almost passivated the ZnO surface states to the largest extent. For the ZnO-CdS-NA sample with $L = 3$ nm, the still rather strong DLE is attributed to the presence of some ZnO regions not well passivated by formation of CdS quantum dot monolayer (Figure S2, Supporting Information). The origins for the blue-shifted and weakened NBE emission, as well as the blue shift in DLE, upon increasing L may be related to the sulfur-doping effect resulting from further diffusion of surface sulfur atoms into inside ZnO nanorod.[36,37] Note the weakened NBE emission could also be partially related to the interfacial charge transfer with some holes in ZnO migrating favorably into CdS.[33,34]

Figure S3 (Supporting Information) clearly shows that MEH-PPV can well infiltrate into the interspaces between either ZnO-NA or ZnO-CdS-NA nanorods after thermal annealing (150 °C, 20 min). MEH-PPV/ZnO-NA and MEH-PPV/ZnO-CdS-NA composite films were characterized by absorption and room temperature PL spectra (Figure 5). The
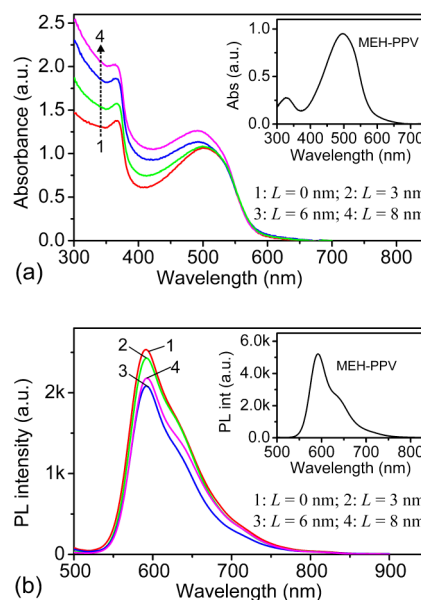

Figure 5. (a) Absorption and (b) room temperature PL (excited at 480 nm) spectra of the composite films based on MEH-PPV and TiO$_2$-NA ($L = 0$ nm) and ZnO-CdS-NA with $L = 3$, 6, or 8 nm. The insets to (a) and (b) are the absorption and room temperature PL spectra of MEH-PPV film on glass substrate.

MEH-PPV/ZnO-NA film exhibits the absorption onset at 388 nm corresponding to ZnO band gap (Figure 4a) and the π–π^* band absorption of MEH-PPV in 400–600 nm (inset to Figure 5a); however, the MEH-PPV/ZnO-CdS-NA films exhibit the enhanced absorption of ZnO and MEH-PPV with increasing L, consistent with the absorption features of ZnO-CdS-NA samples (Figure 4a). The PL spectra of all the composite films (Figure 5b) display the emission profiles similar to those of the pristine MEH-PPV (inset to Figure 5b), suggesting that the remaining luminescence in them is due to the radiative decay of the excitons from MEH-PPV. As shown previously,[15,38] an effective charge transfer from MEH-PPV to ZnO nanorods occurs in the MEH-PPV/ZnO-NA composites as a result of the exciton dissociation at MEH-PPV/ZnO interface, leading to the quenched PL emission of the polymer. By

comparing the maximum emission intensity of the composites to that of pristine MEH-PPV film, we calculated the efficiency (QE) for nanoarray to quench polymer PL emission. The QE for the pristine ZnO-NA was 51%. With CdS shell formation, the QE initially get increased to 53% (L = 3 nm) and 60% (L = 6 nm), but further increasing L up to 8 nm leads to a slightly decreased rather than increased QE (i.e., 58%). The slightly enhanced QE values with increasing L from 0 to 6 nm are attributed to the enlarged D/A interface area for exciton dissociation due to the increased nanorod diameter upon the CdS shell formation. The small decrease by 2% in QE for increasing L from 6 to 8 nm reflects that more polymer excitons relax to the ground state by radiative decay before reaching the D/A interface within their lifetimes, which is caused by the reduced polymer amount between nanorods (refer to Figure 7b). Generally, the QE values for L = 0−8 nm are comparable; in particular, the almost unchanged QE value for L = 0 and 3 nm is observed when the nanorod diameter influence is rather small. These PL results inform that the CdS shell formation does not alter remarkably the efficiency of energy transfer from MEH-PPV to nanorods, and the MEH-PPV/CdS and MEH-PPV/ZnO interfaces are similarly effective for dissociating the polymer excitons.

3.2. Solar Cells. Figure 6a shows the steady-state J−V characteristics related to L values in the solar cells. Table 1
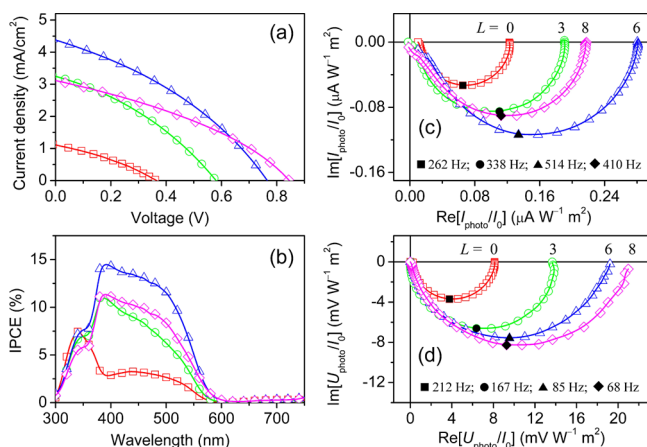

Figure 6. Typical J−V (a), IPCE (b), IMPS (c) and IMVS (d) spectra of the solar cells based on ZnO-NA (□) and ZnO-CdS-NA with L = 3 (○), 6 (△), or 8 (◇) nm. The solid symbols on (c) and (d) identify the f_{min} points.

presents the overall photovoltaic performance of these devices. The overall performance of MEH-PPV/ZnO-NA (i.e., L = 0 nm) solar cells is comparable to the previous reports based on the similarly grown ZnO-NA.[14,19,39] With the CdS shell formation, the device J_{sc} initially increases from 1.22 mA/cm^2 (L = 0 nm) to 4.65 mA/cm^2 for L = 6 nm, but further increasing L leads to a decrease in J_{sc}; moreover, the device V_{oc}

is increased rapidly as L increases from 0 to 6 nm, and further increasing L up to 8 nm only results in a slight increase in V_{oc}. Except for the similar fill factor (FF) of around 34%, both J_{sc} and V_{oc} of MEH-PPV/ZnO-CdS-NA devices are significantly L-dependent, resulting in a peak power conversion efficiency of η = 1.23% under AM 1.5 illumination (100 mW/cm^2) for L = 6 nm, which is ca. 7-fold higher than that of MEH-PPV/ZnO-NA devices. The dependences of J_{sc} and V_{oc} on CdS shell thickness are similar to those on the CdS amount in CdS-sensitized MEH-PPV/ZnO-NA devices,[19] but the peak efficiency, and J_{sc} as well, in our case are nearly 1-fold higher.

As shown in Figure 6b, the MEH-PPV/ZnO-NA device exhibits an IPCE peak at ∼340 nm due to the photocurrent generated by ZnO component and a broad peak within 400−600 nm (centered around 475 nm) for the photocurrent produced by MEH-PPV, where the spectral response in the visible region is quite low, indicating that the excitons generated in MEH-PPV are not efficiently converted into photocurrent. In MEH-PPV/ZnO-CdS-NA devices, however, there is an IPCE peak at ca. 390 nm due to CdS abosrption,[19,20] in addition to the contributions from MEH-PPV and ZnO components. Compared to the MEH-PPV/ZnO-NA solar cells, the MEH-PPV/ZnO-CdS-NA devices show a much higher IPCE in the range of 400−600 nm, in agreement with the increased absorption by CdS up to 550 and even 600 nm (Figures 4a and 5a). The IPCE becomes enhanced with increasing L from 0 to 6 nm, but further increasing L to 8 nm results in a decreased IPCE. The L-dependence of IPCE is the same to that of J_{sc}.

To get insight into the effects of CdS shell layer on device performance, the dynamic studies of solar cells were carried out using IMPS and IMVS techniques. As powerful dynamic photoelectrochemical methods, IMPS and IMVS have been widely applied to study the charge generation and transport dynamics in dye-sensitized solar cells (DSCs).[40−53] Recently, we have applied successfully IMPS and IMVS methods to hybrid PSCs.[15,26,38,54] IMPS/IMVS measures the photocurrent/photovoltage response to a small sinusoidal light perturbation ($I_{ac}=I_0\delta e^{i\omega t}$) superimposed on the background light intensity I_0 under short-circuit/open-circuit condition. The measured IMPS or IMVS responses appear in the fourth quadrant (positive real, negative imaginary) of the complex plane with a shape of distorted semicircle (Figure 6c,d), similar to the previous observations on DSCs and PSCs. The L influences on the device photocurrent (I_{photo}) and photovoltage (U_{photo}) are the same to those on J_{sc} and V_{oc}. On the other hand, the time constant τ defined by the frequency (f_{min}) of the lowest imaginary component of IMPS or IMVS response is an evaluation of the transit time τ_D for the electrons to reach the collection electrode under short-circuit condition or the electron lifetime τ_e related to interfacial charge recombination under open-circuit condition. According to the relation $\tau = (2\pi f_{min})^{-1}$, τ_D and τ_e in the devices were calculated (Table 1),

Table 1. Device Performance of MEH-PPV/ZnO-NA (L = 0 nm) and MEH-PPV/ZnO-CdS-NA (L = 3−8 nm) Solar Cells[a]

L (nm)	V_{oc} (V)	J_{sc} (mA/cm^2)	FF (%)	η (%)	τ_D (ms)	τ_e (ms)
0	0.36 ± 0.03	1.22 ± 0.16	33.03 ± 1.36	0.15 ± 0.04	0.66 ± 0.09	0.76 ± 0.01
3	0.58 ± 0.02	3.12 ± 0.50	34.73 ± 0.25	0.63 ± 0.11	0.45 ± 0.05	1.03 ± 0.13
6	0.77 ± 0.01	4.65 ± 0.58	34.40 ± 1.05	1.23 ± 0.13	0.31 ± 0.00	1.74 ± 0.21
8	0.82 ± 0.02	3.10 ± 0.12	33.73 ± 1.53	0.87 ± 0.05	0.39 ± 0.00	2.18 ± 0.27

[a]Each of the data with standard deviations represents the average of three devices.

where the data for the ZnO-NA device are comparable to our previous results.[54] τ_D decreases when increasing L from 0 to 6 nm but remarkably increases upon further increasing L to 8 nm; however, τ_e keeps increasing with increasing L from 0 to 8 nm. The reduced τ_D suggests an easier transport of electrons to collection electrode, whereas the increased τ_e infers a reduced interfacial charge recombination.

Figure 7a shows the band structure in the MEH-PPV/ZnO-CdS-NA solar cells, in which MEH-PPV, CdS, and ZnO form
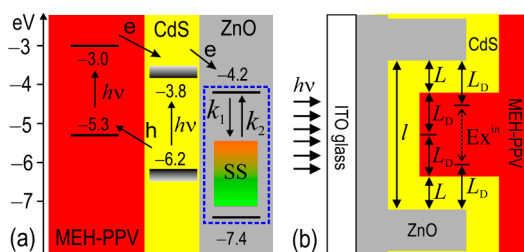

Figure 7. (a) Schematic illustration of the band structure in MEH-PPV/ZnO-CdS-NA devices, where broad conduction and valence band energy levels for CdS indicate the band gap expansion due to the quantum size effect, and the dotted frame indicates that the electrons injected into the conduction band of ZnO may be trapped (k_1) by surface defect states (SS) and the trapped electrons can be thermally released (k_2) into the conduction band. (b) Illustration of the regions (Ex^{in}) with polymer excitons ineffective for charge generation existing between the ZnO nanorods interspaced by a distance of l nm in ZnO-NA solar cells ($L = 0$ nm) and absence of the Ex^{in} regions between ZnO/CdS-core/shell nanorods in ZnO-CdS-NA devices as $L + L_D = l/2$, where L_D means the exciton diffusion length in polymer phase.

type II heterojunctions with staggered band alignments.[19,20] Accordingly, the excitons generated in MEH-PPV dissociate at the MEH-PPV/CdS interface by injecting electrons into CdS and further into ZnO with holes remaining in MEH-PPV; in addition, the excitons generated in CdS dissociate at the ZnO/CdS interface by injecting electrons into ZnO with holes injected into the polymer. As depicted in Figure 1, the photogenerated electrons are transported toward the collection electrode (i.e., ITO) by ZnO-NA for photocurrent generation.

IMPS and IMVS data clearly show that CdS shell formation on ZnO nanorods significantly alters the transport (τ_D) and recombination (τ_e) dynamics of photogenerated electrons (Table 1). It should be rationalized that the transport and recombination dynamics detected by IMPS and IMVS are related to the electrons in ZnO nanorod cores. Using the electron mobility $\mu_e = (0.5-4) \times 10^{-2}$ cm^2 V^{-1} s^{-1} obtained in chemically deposited CdS films,[55,56] the electron diffusion coefficient D_e in the CdS shell layer is estimated to be $10^{-4}-10^{-3}$ cm^2/s according to Einstein relation $qD_e = k_B T\mu_e$, where q is the elementary charge, k_B is the Boltzmann constant, and T is the absolute temperature. The time t for electrons to diffuse across the CdS shell with $L = 3-10$ nm is approximately within 0.1−10 ns according to the relationship $t = L^2/D_e$;[47–53] in addition, previous results have demonstrated that charge injection from CdS into ZnO normally occurs ultrafast on a time scale from picoseconds up to nanoseconds.[57,58] Therefore, the experimental τ_D reasonably reflects the transport of photogenerated electrons in ZnO nanorods. Furthermore, because the back electron transfer from ZnO into the CdS conduction band is impossible due to an unfavorable band structure for such action (Figure 7a), the electrons injected into

the ZnO nanorods at open circuit eventually undergo the charge recombination at the ZnO/CdS interfaces.

3.2.1. CdS Effects on Exciton and Charge Generation. The exciton generation and dissociation are two crucial steps for efficient photocurrent generation in PSCs. As shown previously,[26,38] the charge generation in MEH-PPV/ZnO-NA solar cells dominantly correlates with the polymer excitons generated in the interspaces between ZnO nanorods with a length around 400−500 nm, for which the exciton dissociation at the MEH-PPV/ZnO interface provided by ZnO nanorod side face plays a dominant role. Due to the short exciton diffusion length (L_D) in MEH-PPV (~5−8 nm),[59–61] therefore, only excitons within the exciton diffusion length of the MEH-PPV/ZnO interface lead to separated charges. Statistically, about 80% ZnO nanorods are in a diameter range of 22−32 nm and the averaged diameter of ZnO nanorods is about 28 nm in this experiment (Figure S4, Supporting Information). The interspacing (l) between the ZnO nanorods is statistically averaged to be $l \approx 25$ nm, which agrees with the previous reports by others.[27] Because $L_D < l/2$, there exists actually an Ex^{in} region in the polymer phase between two ZnO nanorods, in which excitons are ineffective for charge generation because they cannot reach the MEH-PPV/ZnO interface for dissociation within their lifetimes. The model concerning the Ex^{in} regions in MEH-PPV/ZnO-NA solar cells with $L = 0$ nm is schematically depicted in Figure 7b, where the ZnO nanorods are assumed to be aligned vertically and orderly on the dense ZnO layer.[26]

In the MEH-PPV/ZnO-CdS-NA devices, derived from the assumed ZnO-NA (Figure 7b) by CdS shell formation with a CdS layer thickness of L nm, the excitons generated in MEH-PPV can be efficiently dissociated at MEH-PPV/CdS interface (Figure 5b) and the MEH-PPV between ZnO/CdS-core/shell nanorods still contributes significantly to charge generation.[62] Clearly, the Ex^{in} regions between the core/shell nanorods will also be present for $L + L_D < l/2$ but will disappear as $L + L_D = l/2$ (Figure 7b). Increasing L within the range of $L + L_D \leq l/2$ will not affect the population of the effective excitons in MEH-PPV for charge generation, because the reduced MEH-PPV amount between the core/shell nanorods is actually related to the production of inefficient excitons; further increasing L up to $L + L_D > l/2$, however, reduces the MEH-PPV contribution to charge generation as a result of the decreased effective excitons in the polymer phase.

Considering that the exciton generation in CdS shell gets increased with increasing L due to the enhanced CdS absorption (Figures 4a and 5a), which results in a nontrivial contribution from CdS,[19,20] it is concluded that the exciton generation and thereby charge generation in MEH-PPV/ZnO-CdS-NA devices will be increased upon formation of CdS shells with $L + L_D \leq l/2$ by generating more CdS excitons without remarkable influence on MEH-PPV contribution but will be a competitive result of increased CdS excitons and decreased effective excitons in MEH-PPV as $L + L_D > l/2$. Because the absorption coefficient of MEH-PPV ($\alpha = 10^5$ cm^{-1}) is 1 order magnitude higher than that of CdS ($\alpha = 10^4$ cm^{-1}),[63] the reduced MEH-PPV contribution will inevitably suppress the increased CdS contribution. Using $l \approx 25$ nm for original ZnO-NA and $L_D \approx 5-8$ nm for MEH-PPV, it is theoretically expected that there exists an optimal L value in the range of $L \approx 4-8$ nm, above which the exciton generation and thereby charge generation in the MEH-PPV/ZnO-CdS-NA solar cells will be reduced. This expectation is confirmed by the presence

of $L = 6$ nm for a peak J_{sc} (Table 1) and IPCE (Figure 6b). Therefore, MEH-PPV absorption still dominantly governs the charge generation in MEH-PPV/ZnO-CdS-NA devices, and the CdS shell can affect the exciton generation and thereby charge generation in the devices by providing additional absorption and reducing polymer contribution. The reduced rather than increased IPCE at 390 nm due to CdS absorption with increasing L from 6 to 8 nm (Figure 6b) provides an additional experimental evidence for the dominant contribution from MEH-PPV absorption.

3.2.2. CdS Effects on J_{sc} and τ_D. The L-dependences of J_{sc} and τ_D are depicted in Figure 8. Clearly, J_{sc} has an L-
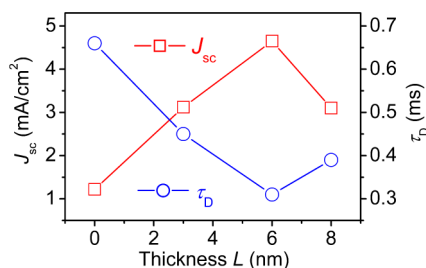

Figure 8. Dependences of averaged J_{sc} and τ_D on CdS shell thickness.

dependence opposite to that of τ_D, with a shorter τ_D for a larger J_{sc}. As the CdS shell imposes very limited influence on the efficiency of energy transfer from MEH-PPV to nanorods (Figure 5b), the L-dependence of J_{sc} is reasonably not originating from the dissociation efficiency of the polymer excitons. Moreover, the photogenerated electrons require the collection at electrode for efficient photocurrent generation. The electron diffusion length (l_D) can be evaluated from the measured τ_e [i.e., $l_D = (D_e \tau_e)^{1/2}$].[47-53] Given $D_e = 10^{-4}$ cm^2/s for nanostructured ZnO,[64] the l_D is estimated to be in the range 2.8−4.7 μm for $\tau_e = 0.76$−2.18 ms (Table 1). Thereby, all the photogenerated electrons are able to be collected in our devices, because the 400 nm distance (i.e., nanorod length) for electrons to diffuse toward collection electrode is much shorter than l_D. Hence, the L-dependence of J_{sc} is related to charge generation rather than either the polymer exciton dissociation or electron collection. Reasonably, the J_{sc} in MEH-PPV/ZnO-CdS-NA devices mainly correlates with the charge generation subjected to the exciton generation altered by CdS shell formation (Figure 7b), in which the polymer absorption is dominantly contributive. The L-dependence of J_{sc} can be explained by the proposed model (Figure 7b). The enhanced J_{sc} (Table 1 and Figure 8) and IPCE (Figure 6b) for increasing L from 0 to 6 nm are due to the increased contribution from CdS absorption when the polymer contribution is almost not affected; however, the reduced rather than increased J_{sc} and IPCE for increasing L from 6 to 8 nm are attributed to the reduced effective amount of MEH-PPV between nanorods,[19] because the increased CdS contribution cannot compensate the loss of effective excitons in MEH-PPV.

Now, let us discuss the electron transit time (τ_D). Surface defects on ZnO nanorod surfaces will strongly affect the transport[65,66] kinetics of photogenerated electrons by trapping/detrapping processes (Figure 7a). As more electrons are trapped by surface defects, they will spend a larger τ_D in transporting to collection electrode. The changing trend in τ_D for increasing L from 0 to 6 nm agrees with the reduced defect concentration on ZnO nanorods (inset to Figure 4b); however,

the samples with $L = 6$ and 8 nm have a comparable ZnO surface defect concentration, but their τ_D values differ significantly. Therefore, the L-dependences of τ_D cannot be well accounted for by the change in ZnO surface defect concentration. Actually, the electron diffusion coefficient correlates with the electron concentration in conduction band.[45,46,52] For example, ZnO-CdS core/shell nanorods have a much higher conductance than the pristine ZnO nanorods due to the additional electron injection from the CdS shell.[36] The changes in τ_D values upon CdS shell formation correlate evidently with the L-dependent electron concentration in the ZnO conduction band, for which the photocurrent may act as a rough measure (Figure 8). Note, the reduced surface defects on ZnO for trapping electrons, and the reduced charge recombination as well (Table 1), will also allow more photogenerated electrons to accommodate in the ZnO conduction band, favoring the increases in the electron concentration therein and the device J_{sc}. Obviously, in comparison to J_{sc} for MEH-PPV/ZnO-CdS-NA devices, the much poorer J_{sc} in MEH-PPV/ZnO-NA devices is due to the lower charge generation and the rich amount of ZnO deep-level defects for stronger electron trapping and more serious charge recombination.

3.2.3. CdS Effects on τ_e and V_{oc}. Shown in Figure 9 are the L-dependences of V_{oc} and τ_e. Interestingly, either V_{oc} or τ_e data
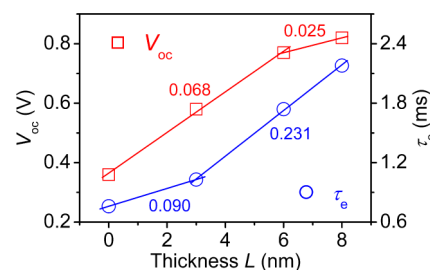

Figure 9. Dependences of averaged V_{oc} and τ_e on CdS shell thickness. The lines were calculated by linear regression for experimental data expressed by scatters and the numeral marked by each line is the line slope.

are well represented by two lines in the tested L range. These suggest that the CdS shell has different L-dependent effects on either V_{oc} or charge recombination (i.e., τ_e).

3.2.3.1. On τ_e. The increase in τ_e with increasing CdS shell thickness in the range of $L = 0$−3 nm takes place by a small gradient of 0.090 ms/nm, but increasing L from 3 to 8 nm produces the τ_e increase with a much larger gradient (i.e., 0.231 ms/nm). Surface defects on ZnO nanorod surfaces will affect the recombination kinetics of photogenerated electrons by trapping/detrapping processes.[64,67,68] As more electrons are trapped by surface defects (Figure 7a), they will not easily escape from the D/A interface where a substantial number of holes exist, leading to a faster recombination or smaller τ_e. The reduced recombination for increasing L from 0 to 3 nm is reasonably attributed to the reduced ZnO surface defects for trapping electrons upon formation of CdS monolayer, which can be further evidenced to a certain extent by the comparable gradients (Figures 4b and 9) linearly fitted for increasing τ_e (0.090 ms/nm) and decreasing ZnO surface defects (0.093 ms/nm).

On the other hand, in comparison to the cases of $L = 0$−3 nm, increasing L from 3 to 8 nm leads to a smaller decreasing

gradient of ZnO surface defects (Inset to Figure 4b) but a much higher increasing gradient of τ_e (Figure 9). In particular, the τ_e values differ significantly in the devices (i.e., $L = 6$ and 8 nm) with a comparable ZnO surface defect concentration. These results indicate that the τ_e for $L = 3-8$ nm should not be tightly related to the change in ZnO surface defect concentration. In excitonic solar cells, there exists a charge-transfer (CT) state of weakly bound pairs of photogenerated electrons (e) and holes (h) within the e−h separation of a few nanometers by Coulombic attraction.[69−75] The charges in the CT states may either become free charge carriers after overcoming their mutual Coulombic attraction or recombine to loss energy. We believe that the reduced recombination for increasing L from 3 to 8 nm mainly correlates with the barrier effect of CdS shell on the electronic coupling for charge recombination. With the electron injection into ZnO and the migration of holes in the CdS shell toward MEH-PPV, the CdS shell actually acts as a barrier layer to prevent electrons and holes from electronic coupling by increasing the spatial e−h separation.[76,77] The spatial e−h separation inevitably gets increased with increasing L, leading to a weakened e−h coupling for a reduced charge recombination at the ZnO/CdS interface or a larger τ_e. As indicated by the slopes (i.e., 0.090 and 0.231 ms/nm) of the linear regression lines, the CdS shell barrier effect on reducing charge recombination is much stronger than that of the reduced surface defects if L is large enough (e.g., $L > 3$ nm). It should be noted that the effect of reduced ZnO surface defects on reducing charge recombination (i.e., increasing τ_e) will also present for $L = 3-6$ nm, but it is merely surpassed by the barrier effect of CdS shell on the e−h coupling.

3.2.3.2. On V_{oc}. It is still the subject of much debate to understand the factors determining V_{oc} in PSCs. Normally, the V_{oc} correlates with the energy difference between the highest occupied molecular orbital (HOMO) level of the donor and the conduction band edge or lowest unoccupied molecular orbital (LUMO) level of the acceptor.[1−3,69,78,79] The increased V_{oc} upon the CdS deposition in CdS-sensitized MEH-PPV/ZnO-NA devices[19] is attributed to the band offset between CdS and ZnO in the cascading band structure formed upon CdS deposition, which increases the energy difference between the HOMO level of the polymer donor and the conduction band edge of the acceptor.[20] In this experiment, the thinner CdS shell contains more smaller CdS quantum dots than the thicker one (Figures 2f and S1, Supporting Information). The reduction in quantum dot size will shift the conduction band and valence band edges of CdS quantum dots toward and away from vacuum, respectively, resulting in a bang-gap expansion[31] (Figures 4a and 7a). Accordingly, a higher V_{oc} for $L = 3$ nm than $L = 6-8$ nm should be expected, which clearly contradicts the experimental results (Table 1 and Figure 9). Therefore, the band-offset standpoint[19,20] cannot explain the observed L-dependence of V_{oc}. Moreover, a relation between V_{oc} and electron concentration in the conduction band exists in polymer:fullerene solar cells at room temperature,[80] even though the electron concentration cannot explain the saturation of V_{oc} at low temperatures.[81] With the photocurrent as a rough measure (Figure 8), the device with $L = 6$ nm has a higher electron concentration than that of $L = 8$ nm, but the V_{oc} in the latter sample is comparable to or slightly higher than the former one, inferring that the electron concentration is not conclusively responsible for the observed L-dependence of V_{oc}.

Actually, for the devices with specific D and A materials, the V_{oc} is strongly related to the energy difference between the quasi-Fermi levels of the electrons in the A phase and the holes in the D component.[7,8,82,83] According to the energy level diagram of intrinsic defects in the ZnO nanorods synthesized from solution,[84] the zinc vacancy, singly ionized zinc vacancy, and singly ionized oxygen interstitial locate respectively at about 0.28, 0.70, and 0.97 eV above the valence band, but the oxygen vacancy and zinc interstitial locate at ca. 0.05 and 0.42 eV below the conduction band, respectively. The electrons trapped by these surface defect states will have lower quasi-Fermi levels than in the conduction band.[68,85,86] The L-dependence of V_{oc} for $L = 0-6$ nm agrees well with the expectation from the reduced ZnO surface defects, and the linearly fitted gradients for increasing V_{oc} and decreasing ZnO surface defects within the range of $L = 0-6$ nm are very close (Figures 4b and 9); moreover, comparable V_{oc} is observed for $L = 6$ and 8 nm when the ZnO surface defect concentration remains almost unchanged. These experimental results suggest that the L-dependences of V_{oc} have a strong correlation with the ZnO surface defect concentration changed by CdS shell formation. Here, we think that the V_{oc} in the MEH-PPV/ZnO-NA and MEH-PPV/ZnO-CdS-NA devices is determined by the energy levels of conduction band edge in ZnO and HOMO band of MEH-PPV but significantly correlates with the quasi-Fermi levels of the electrons injected into ZnO (Figure 7a). Besides the low J_{sc} (Table 1 and Figure 8), the poor V_{oc} is another factor limiting the efficiency in MEH-PPV/ZnO-NA solar cells. The quite small V_{oc} (i.e., 0.36 V) in the MEH-PPV/ZnO-NA devices is believed to correlate with the rich amount of deep-level defects (e.g., zinc vacancies) on ZnO surfaces that reduce the quasi-Fermi levels of electrons by trapping process. However, in the MEH-PPV/ZnO-CdS-NA devices, as the concentration of the deep-level defects is reduced by formation of CdS shell with $L = 3-6$ nm, more electrons will accommodate in the conduction band of ZnO (Figure 7a), with an increase in the quasi-Fermi level difference between the electrons in ZnO and the holes in MEH-PPV for a higher V_{oc}; the comparable or slightly varied V_{oc} for $L = 6-8$ nm is obviously related to the hardly altered ZnO surface defect concentration as $L \geq 6$ nm (inset to Figure 4b). Actually, the V_{oc} in both ZnO-NA and ZnO-CdS-NA solar cells is influenced by the occupation of injected electrons between the conduction band and surface defects of ZnO nanorods, for which the CdS shell serves as an adjustor.

It is worthy to note that we indeed obtained a small increase in V_{oc} (Table 1 and Figure 9) as the result of increasing L from 6 to 8 nm when the ZnO surface defects have been saturated (Figure 4b). A similar phenomenon was also observed in CdS-sensitized MEH-PPV/ZnO-NA[19] and P3HT/TiO$_2$-Sb$_2$S$_3$-NA[87] devices with different CdS or Sb$_2$S$_3$ loads on ZnO or TiO$_2$ nanorods, but the reason was not clearly understood yet. Besides the factors mentioned above, including the energy difference between D and A components and the quasi-Fermi levels of electrons, the electronic coupling in CT state should also be an important factor influencing V_{oc} in MEH-PPV/ZnO-CdS-NA devices. It has been demonstrated that the energy loss due to the electronic coupling for charge recombination in the CT state reduce the device V_{oc}.[88−90] Increasing L leads to a weakened e−h coupling by increasing the spatial e−h separation, as is indicated by the increased τ_e (Table 1 and Figure 9). Reasonably, although the V_{oc} in MEH-PPV/ZnO-CdS-NA solar cells significantly correlates with the quasi-Fermi

levels of the electrons in ZnO nanorods subjected to varied ZnO surface defects, the electronic coupling effect on V_{oc} is not ignorable, in particular, in the cases with a comparable ZnO surface defect concentration (e.g., L = 6 and 8 nm). The slight increase in V_{oc} for increasing L from 6 to 8 nm is therefore attributed to the weakened e−h coupling for charge recombination. It should also be noted that the reduced e−h coupling effect on improving V_{oc} will also present for L = 3−6 nm but it is merely surpassed by the effect of reduced ZnO surface defects.

3.2.4. Remarks. Almost a monolayer of CdS quantum dots (2−3 nm) is formed for L = 3 nm, whereas thicker CdS shells with L = 6 and 8 nm contain the irregular aggregation of CdS quantum dots (2−5 nm) (Figures 2f and S1, Supporting Information). Transient studies have shown that the aggregation of CdSe quantum dots on ZnO nanorods or TiO$_2$ nanoparticles will lead to the heterogeneous injection of electrons from CdSe into ZnO or TiO$_2$ with a reduced rate (ca. tens to hundreds of picoseconds).[91,92] Here, we do not think the decreased J_{sc} upon increasing L from 6 to 8 nm results from the increased time t for the electrons to diffuse across the CdS shell, because this time (t < 10 ns) is much shorter than the diffusion time of ca. 0.3−0.7 ms in ZnO nanorods (Table 1).

At the first glimpse, on the other hand, increasing L leads to a longer τ_e and a larger V_{oc} (Table 1). Previous reports on PSCs[7−15,93,94] or DSCs[44,95] also show a larger V_{oc} is accompanied by a reduced recombination (or longer τ_e), which seems to inform that τ_e is a decisive factor for the V_{oc} in PSCs[16,19,20] and DSCs.[44,95] In fact, systematical results in PSCs have indicated that no direct correlation exists between V_{oc} on τ_e,[15,18,38,54] even though they may change in a similar trend under the same influencing factor.[15,38,54] The different L-dependences of V_{oc} and τ_e upon CdS shell formation (Figure 9) again confirm that there is no direct correlation between the V_{oc} and τ_e in the MEH-PPV/ZnO-CdS-NA solar cells. Both V_{oc} and τ_e for L = 0−3 nm are mainly influenced by the ZnO surface defect concentration, the V_{oc} is mainly affected by ZnO surface defect concentration but τ_e mainly by the spatial e−h separation for electronic coupling as L = 3−6 nm, but both V_{oc} and τ_e are mainly influenced by the spatial e−h separation in the cases of L = 6−8. These L-dependent influencing factors lead to the observation of the different changing trends in V_{oc} and τ_e upon CdS shell formation. Therefore, we do not think the increased V_{oc} upon formation of the CdS shell is mainly caused by the reduced charge recombination or the larger electron lifetime τ_e.

4. CONCLUSION

For the first time, we show an approach to significantly enhance the performance of MEH-PPV/ZnO-NA hybrid solar cells by formation of ZnO/CdS-core/shell heterostructures, demonstrate the CdS shell effects on the steady-state and dynamic performances (J_{sc}, V_{oc}, τ_D and τ_e), and propose a model concerning the ineffective polymer phase for understanding the charge generation upon CdS shell growth. The poor performance (η = 0.15%) in MEH-PPV/ZnO-NA solar cells is tightly related to low charge generation and the rich amount of deep-level defects on ZnO nanorods. However, in the MEH-PPV/ZnO-CdS-NA devices, the CdS shell formation does not remarkably alter the dissociation efficiency of the polymer excitons but reduces the deficiencies in MEH-PPV/ZnO-NA by imposing the L-dependent effects to improve device performance, including (i) providing additional absorption for exciton generation, (ii) passivating the ZnO surface defects, and (iii) providing a barrier layer to weaken e-h coupling. A peak efficiency of η = 1.23% (AM 1.5, 100 mW/cm^2) is achieved in the MEH-PPV/ZnO-CdS-NA device with L = 6 nm in the tested range. Our results demonstrate the possibility to improve the V_{oc}, J_{sc}, and thereby η in hybrid PSCs by formation of the heterogeneous shell on electron transporter with staggered band alignments; the results here will help to guide the design of materials and architectures in low-cost solar cells.

- The J_{sc} in MEH-PPV/ZnO-CdS-NA devices correlates mainly with the charge generation subjected to the exciton generation altered by CdS shell formation, in which the polymer absorption is dominantly contributive. The observed L-dependence of J_{sc} upon CdS shell formation is well explained by the proposed model. J_{sc} is increased with increasing CdS shell thickness within a suitable range (e.g., L = 3−6 nm), but a thicker CdS shell will reduce J_{sc} by causing the loss of polymer contribution. The optimal CdS thickness of L = 6 nm for a peak J_{sc} is originally determined by the interspacing (l) between ZnO nanorods and the exciton diffusion length L_D in the polymer.

- The τ_D in MEH-PPV/ZnO-CdS-NA devices dominantly correlates with the electron concentration in ZnO conduction band, resulting in the L-dependence of τ_D opposite to that of J_{sc}, i.e., a shorter τ_D for a larger J_{sc}, for which the L-dependent charge generation is mainly responsible with additional contributions from reduced electron trapping and recombination.

- The V_{oc} in the MEH-PPV/ZnO-NA and MEH-PPV/ZnO-CdS-NA devices is determined by the energy levels of the conduction band edge of ZnO and the HOMO band of MEH-PPV but significantly correlates with the quasi-Fermi levels of the electrons injected into ZnO. The CdS shell has two L-dependent effects on improving V_{oc}, that is, to reduce the deep-level surface defects on ZnO nanorods to increase the quasi-Fermi levels of electrons and to weaken the e-h coupling for a higher V_{oc}.

- The τ_e in MEH-PPV/ZnO-CdS-NA devices correlates with the e−h separation for electronic coupling and the ZnO surface defects. The CdS shell mainly reduces the charge recombination (or increases τ_e) by passivating ZnO surface defects as L is rather small, but by weakening the e-h electronic coupling for larger L values (L > 3 nm).

- The different L-dependences of V_{oc} and τ_e subjected to CdS shell formation indicate no direct correlation between V_{oc} and τ_e in MEH-PPV/ZnO-CdS-NA devices.

■ ASSOCIATED CONTENT

Ⓢ Supporting Information

TEM and HRTEM images of the ZnO/CdS-core/shell nanorods with L = 3 and 8 nm; SEM images of MEH-PPV/ZnO-NA and MEH-PPV/ZnO-CdS-NA composite films; statistical distribution of ZnO nanorod diameter in ZnO-NA. This material is available free of charge via the Internet at http://pubs.acs.org.

■ AUTHOR INFORMATION

Corresponding Author
*Tel/Fax: 0086-551-65593171. E-mail: mtwang@ipp.ac.cn.

Notes

The authors declare no competing financial interest.

■ REFERENCES

(1) Günes, S.; Neugebauer, H.; Sariciftci, N. S. Conjugated Polymer-Based Organic Solar Cells. *Chem. Rev.* **2007**, *107*, 1324−1338.

(2) Skompska, M. Hybrid Conjugated Polymer/Semiconductor Photovoltaic Cells. *Synth. Met.* **2010**, *160*, 1−15.

(3) Xu, T.; Qiao, Q. Conjugated Polymer−Inorganic Semiconductor Hybrid Solar Cells. *Energy Environ. Sci.* **2011**, *4*, 2700−2720.

(4) Gonzalez-Valls, I.; Lira-Cantu, M. Vertically-Aligned Nanostructures of ZnO for Excitonic Solar Cells: A Review. *Energy Environ. Sci.* **2009**, *2*, 19−34.

(5) Huang, J.; Yin, Z.; Zheng, Q. Applications of ZnO in Organic and Hybrid Solar Cells. *Energy Environ. Sci.* **2011**, *4*, 3861−3877.

(6) Weickert, J.; Dunbar, R. B.; Hesse, H. C.; Wiedemann, W.; Schmidt-Mende, L. Nanostructured Organic and Hybrid Solar Cells. *Adv. Mater.* **2011**, *23*, 1810−1828.

(7) Lin, Y.-Y.; Chu, T.-H.; Li, S.-S.; Chuang, C.-H.; Chang, C.-H.; Su, W.-F.; Chang, C.-P.; Chu, M.-W.; Chen, C.-W. Interfacial Nanostructuring on the Performance of Polymer/TiO₂ Nanorod Bulk Heterojunction Solar Cells. *J. Am. Chem. Soc.* **2009**, *131*, 3644−3649.

(8) Goh, C.; Scully, S. R.; McGehee, M. D. Effects of Molecular Interface Modification in Hybrid Organic-Inorganic Photovoltaic Cells. *J. Appl. Phys.* **2007**, *101*, 114503.

(9) Kudo, N.; Honda, S.; Shimazaki, Y.; Ohkita, H.; Ito, S.; Benten, H. Improvement of Charge Injection Efficiency in Organic-Inorganic Hybrid Solar Cells by Chemical Modification of Metal Oxides with Organic Molecules. *Appl. Phys. Lett.* **2007**, *90*, 183513.

(10) Lin, Y.-Y.; Chu, T.-H.; Chen, C.-W.; Su, W.-F. Improved Performance of Polymer/TiO₂ Nanorod Bulk Heterojunction Photovoltaic Devices by Interface Modification. *Appl. Phys. Lett.* **2008**, *92*, 053312.

(11) Jiang, K.-J.; Manseki, K.; Yu, Y.-H.; Masaki, N.; Suzuki, K.; Song, Y.-L.; Yanagida, S. Photovoltaics Based on Hybridization of Effective Dye-Sensitized Titanium Oxide and Hole-Conductive Polymer P3HT. *Adv. Funct. Mater.* **2009**, *19*, 2481−2485.

(12) Said, A. J.; Poize, G.; Martini, C.; Ferry, D.; Marine, W.; Giorgio, S.; Fages, F.; Hocq, J.; Bouclé, J.; Nelson, J.; et al. Hybrid Bulk Heterojunction Solar Cells Based on P3HT and Porphyrin-Modified ZnO Nanorods. *J. Phys. Chem. C* **2010**, *114*, 11273−11278.

(13) Peiró, A. M.; Ravirajan, P.; Govender, K.; Boyle, D. S.; O'Brien, P.; Bradley, D. D. C.; Nelson, J.; Durrant, J. R. Hybrid Polymer/Metal Oxide Solar Cells Based on ZnO Columnar Structures. *J. Mater. Chem.* **2006**, *16*, 2088−2096.

(14) Ravirajan, P.; Peiró, A. M.; Nazeeruddin, M. K.; Graetzel, M.; Bradley, D. D. C.; Durrant, J. R.; Nelson, J. Hybrid Polymer/Zinc Oxide Photovoltaic Devices with Vertically Oriented ZnO Nanorods and an Amphiphilic Molecular Interface Layer. *J. Phys. Chem. B* **2006**, *110*, 7635−7639.

(15) Bi, D.; Wu, F.; Qu, Q.; Yue, W.; Cui, Q.; Shen, W.; Chen, R.; Liu, C.; Qiu, Z.; Wang, M. Device Performance Related to Amphiphilic Modification at Charge Separation Interface in Hybrid Solar Cells with Vertically Aligned ZnO Nanorod Arrays. *J. Phys. Chem. C* **2011**, *115*, 3745−3752.

(16) Greene, L. E.; Law, M.; Yuhas, B. D.; Yang, P. ZnO−TiO₂ Core−Shell Nanorod/P3HT Solar Cells. *J. Phys. Chem. C* **2007**, *111*, 18451−18456.

(17) Lee, Y.-J.; Lloyd, M. T.; Olson, D. C.; Grubbs, R. K.; Lu, P.; Davis, R. J.; Voigt, J. A.; Hsu, J. W. P. Optimization of ZnO Nanorod Array Morphology for Hybrid Photovoltaic Devices. *J. Phys. Chem. C* **2009**, *113*, 15778−15782.

(18) Lee, Y.-J.; Davis, R. J.; Lloyd, M. T.; Provencio, P. P.; Prasankumar, R. P.; Hsu, J. W. P. Open-Circuit Voltage Improvement in Hybrid ZnO−Polymer Photovoltaic Devices with Oxide Engineering. *IEEE J. Sel. Top. Quantum Electron.* **2010**, *16*, 1587−1594.

(19) Wang, L.; Zhao, D.; Su, Z.; Li, B.; Zhang, Z.; Shen, D. Enhanced Efficiency of Polymer/ZnO Nanorods Hybrid Solar Cell Sensitized by CdS Quantum Dots. *J. Electrochem. Soc.* **2011**, *158*, H804−H807.

(20) Spoerke, E. D.; Lloyd, M. T.; McCready, E. M.; Olson, D. C.; Lee, Y.-J.; Hsu, J. W. P. Improved Performance of Poly(3-hexylthiophene)/Zinc Oxide Hybrid Photovoltaics Modified with Interfacial Nanocrystalline Cadmium Sulfide. *Appl. Phys. Lett.* **2009**, *95*, 213506.

(21) Tak, Y.; Hong, S. J.; Lee, J. S.; Yong, K. Fabrication of ZnO/CdS Core/Shell Nanowire Arrays for Efficient Solar Energy Conversion. *J. Mater. Chem.* **2009**, *19*, 5945−5951.

(22) Guerguerian, G.; Elhordoy, F.; Pereyra, C. J.; Marotti, R. E.; Martín, F.; Leinen, D.; Ramos-Barrado, J. R.; Dalchiele, E. A. ZnO Nanorod/CdS Nanocrystals Core/Shell-Type Heterostructures for Solar Cell Applications. *Nanotechnology* **2011**, *22*, 505401.

(23) Yao, C.-Z.; Wei, B.-H.; Meng, L.-X.; Li, H.; Gong, Q.-J.; Sun, H.; Ma, H.-X.; Hu, X.-H. Controllable Electrochemical Synthesis and Photovoltaic Performance of ZnO/CdS Core−Shell Nanorod Arrays on Fluorine-Doped Tin Oxide. *J. Power Sources* **2012**, *207*, 222−228.

(24) Nayak, J. Enhanced Light to Electricity Conversion Efficiency of CdS−ZnO Composite Nanorod Based Electrochemical Solar Cell. *Mater. Chem. Phys.* **2012**, *133*, 523−527.

(25) Sun, B.; Hao, Y.; Guo, F.; Cao, Y.; Zhang, Y.; Li, Y.; Xu, D. Fabrication of Poly(3-hexylthiophene)/CdS/ZnO Core−Shell Nanotube Array for Semiconductor-Sensitized Solar Cell. *J. Phys. Chem. C* **2012**, *116*, 1395−1400.

(26) Wu, F.; Shen, W.; Cui, Q.; Bi, D.; Yue, W.; Qu, Q.; Wang, M. Dynamic Characterization of Hybrid Solar Cells Based on Polymer and Aligned ZnO Nanorods by Intensity Modulated Photocurrent Spectroscopy. *J. Phys. Chem. C* **2010**, *114*, 20225−20235.

(27) Greene, L. E.; Law, M.; Tan, D. H.; Montano, M.; Goldberger, J.; Somorjai, G.; Yang, P. General Route to Vertical ZnO Nanowire Arrays Using Textured ZnO Seeds. *Nano Lett.* **2005**, *5*, 1231−1236.

(28) Zhang, Y.; Xie, T.; Jiang, T.; Wei, X.; Pang, S.; Wang, X.; Wang, D. Surface Photovoltage Characterization of A ZnO Nanowire Array/CdS Quantum Dot Heterogeneous Film and Its Application for Photovoltaic Devices. *Nanotechnology* **2009**, *20*, 155707.

(29) Song, X.; Fu, Y.-S.; Xie, Y.; Song, J.-G.; Wang, H.-L.; Sun, J.; Du, X.-W. The Effect of Post-Annealing on the Conversion Efficiency of Solar Cells Sensitized by CdS Quantum Dots. *Semicond. Sci. Technol.* **2010**, *25*, 045031.

(30) Vossmeyer, T.; Katsikas, L.; Gienig, M.; Popovic, I. G.; Diesner, K.; Chemseddine, A.; Eychmüller, A.; Weller, H. CdS Nanoclusters: Synthesis, Characterization, Size Dependent Oscillator Strength, Temperature Shift of the Excitonic Transition Energy, and Reversible Absorbance Shift. *J. Phys. Chem.* **1994**, *98*, 7665−7673.

(31) Lang, X. Y.; Zheng, W. T.; Jiang, Q. Finite-Size Effect on Band Structure and Photoluminescence of Semiconductor Nanocrystals. *IEEE Trans. Nanotechnol.* **2008**, *7*, 5−9.

(32) Willander, M.; Nur, O.; Zhao, Q. X.; Yang, L. L.; Lorenz, M.; Cao, B. Q.; Pérez, J. Z.; Czekalla, C.; Zimmermann, G.; Grundmann, M.; et al. Zinc Oxide Nanorod Based Photonic Devices: Recent Progress in Growth, Light Emitting Diodes and Lasers. *Nanotechnology* **2009**, *20*, 332001.

(33) Fang, F.; Zhao, D. X.; Li, B. H.; Zhang, Z. Z.; Zhang, J. Y.; Shen, D. Z. The Enhancement of ZnO Nanowalls Photoconductivity Induced by CdS Nanoparticle Modification. *Appl. Phys. Lett.* **2008**, *93*, 233115.

(34) Villani, M.; Calestani, D.; Lazzarini, L.; Zanotti, L.; Mosca, R.; Zappettini, A. Extended Functionality of ZnO Nanotetrapods by Solution-Based Coupling with CdS Nanoparticles. *J. Mater. Chem.* **2012**, *22*, 5694−5699.

(35) Kundu, P.; Deshpande, P. A.; Madras, G.; Ravishankar, N. Nanoscale ZnO/CdS Heterostructures with Engineered Interfaces for High Photocatalytic Activity under Solar Radiation. *J. Mater. Chem.* **2011**, *21*, 4209−4216.

(36) Gao, T.; Li, Q.; Wang, T. Sonochemical Synthesis, Optical Properties, and Electrical Properties of Core/Shell-Type ZnO Nanorod/CdS Nanoparticle Composites. *Chem. Mater.* **2005**, *17*, 887−892.

(37) Geng, B. Y.; Wang, G. Z.; Jiang, Z.; Xie, T.; Sun, S. H.; Meng, G. W.; Zhang, L. D. Synthesis and Optical Properties of S-Doped ZnO Nanowires. *Appl. Phys. Lett.* **2003**, *82*, 4791−4793.

(38) Bi, D.; Wu, F.; Yue, W.; Guo, Y.; Shen, W.; Peng, R.; Wu, H.; Wang, X.; Wang, M. Device Performance Correlated with Structural Properties of Vertically Aligned Nanorod Arrays in Polymer/ZnO Solar Cells. *J. Phys. Chem. C* **2010**, *114*, 13846−13852.

(39) Olson, D. C.; Shaheen, S. E.; Collins, R. T.; Ginley, D. S. The Effect of Atmosphere and ZnO Morphology on the Performance of Hybrid Poly(3-hexylthiophene)/ZnO Nanofiber Photovoltaic Devices. *J. Phys. Chem. C* **2007**, *111*, 16670−16678.

(40) Dloczik, L.; Ileperuma, O.; Lauermann, I.; Peter, L. M.; Ponomarev, E. A.; Redmond, G.; Shaw, N. J.; Uhlendorf, I. Dynamic Response of Dye-Sensitized Nanocrystalline Solar Cells: Characterization by Intensity-Modulated Photocurrent Spectroscopy. *J. Phys. Chem. B* **1997**, *101*, 10281−10289.

(41) Grasso, C.; Nanu, M.; Goossens, A.; Burgelman, M. Electron Transport in CuInS$_2$-Based Nanostructured Solar Cells. *Thin Solid Films* **2005**, *480−481*, 87−91.

(42) Zhang, D.; Yoshida, T.; Oekermann, T.; Furuta, K.; Minoura, H. Room-Temperature Synthesis of Porous Nanoparticulate TiO$_2$ Films for Flexible Dye-Sensitized Solar Cells. *Adv. Funct. Mater.* **2006**, *16*, 1228−1234.

(43) Lee, B.-K.; Kim, J.-J. Enhanced Efficiency of Dye-Sensitized Solar Cells by UV-O$_3$ Treatment of TiO$_2$ Layer. *Curr. Appl. Phys.* **2009**, *9*, 404−408.

(44) Hara, K.; Miyamoto, K.; Abe, Y.; Yanagida, M. Electron Transport in Coumarin-Dye-Sensitized Nanocrystalline TiO$_2$ Electrodes. *J. Phys. Chem. B* **2005**, *109*, 23776−23778.

(45) Peter, L. M. Characterization and Modeling of Dye-Sensitized Solar Cells. *J. Phys. Chem. C* **2007**, *111*, 6601−6612.

(46) Peter, L. M. Dye-Sensitized Nanocrystalline Solar Cells. *Phys. Chem. Chem. Phys.* **2007**, *9*, 2630−2642.

(47) Peter, L. M.; Wijayantha, K. G. U. Intensity Dependence of the Electron Diffusion Length in Dye-Sensitised Nanocrystalline TiO$_2$ Photovoltaic Cells. *Electrochem. Commun.* **1999**, *1*, 576−580.

(48) Franco, G.; Peter, L. M.; Ponomarev, E. A. Detection of Inhomogeneous Dye Distribution in Dye Sensitized Nanocrystalline Solar Cells by Intensity Modulated Photocurrent Spectroscopy (IMPS). *Electrochem. Commun.* **1999**, *1*, 61−64.

(49) Fisher, A. C.; Peter, L. M.; Ponomarev, E. A.; Walker, A. B.; Wijayantha, K. G. U. Intensity Dependence of the Back Reaction and Transport of Electrons in Dye-Sensitized Nanocrystalline TiO$_2$ Solar Cells. *J. Phys. Chem. B* **2000**, *104*, 949−958.

(50) Krüger, J.; Plass, R.; Grätzel, M.; Cameron, P. J.; Peter, L. M. Charge Transport and Back Reaction in Solid-State Dye-Sensitized Solar Cells: A Study Using Intensity-Modulated Photovoltage and Photocurrent Spectroscopy. *J. Phys. Chem. B* **2003**, *107*, 7536−7539.

(51) Oekermann, T.; Zhang, D.; Yoshida, T.; Minoura, H. Electron Transport and Back Reaction in Nanocrystalline TiO$_2$ Films Prepared by Hydrothermal Crystallization. *J. Phys. Chem. B* **2004**, *108*, 2227−2235.

(52) Bisquert, J.; Vikhrenko, V. S. Interpretation of the Time Constants Measured by Kinetic Techniques in Nanostructured Semiconductor Electrodes and Dye-Sensitized Solar Cells. *J. Phys. Chem. B* **2004**, *108*, 2313−2322.

(53) Dunn, H. K.; Peter, L. M. How Efficient Is Electron Collection in Dye-Sensitized Solar Cells? Comparison of Different Dynamic Methods for the Determination of the Electron Diffusion Length. *J. Phys. Chem. C* **2009**, *113*, 4726−4731.

(54) Wu, F.; Yue, W.; Cui, Q.; Liu, C.; Qiu, Z.; Shen, W.; Zhang, H.; Wang, M. Performance Correlated with Device Layout and Illumination Area in Solar Cells Based on Polymer and Aligned ZnO Nanorods. *Sol. Energy* **2012**, *86*, 1459−1469.

(55) Saad, M.; Kassis, A. Analysis of Illumination-Intensity-Dependent *J−V* Characteristics of ZnO/CdS/CuGaSe$_2$ Single Crystal Solar Cells. *Sol. Energy Mater. Sol. Cells* **2003**, *77*, 415−422.

(56) Nan, Y.-X.; Chen, F.; Yang, L.-G.; Chen, H.-Z. Electrochemical Synthesis and Charge Transport Properties of CdS Nanocrystalline Thin Films with a Conifer-like Structure. *J. Phys. Chem. C* **2010**, *114*, 11911−11917.

(57) Hotchandani, S.; Kamat, P. V. Charge-Transfer Processes in Coupled Semiconductor Systems. Photochemistry and Photoelectrochemistry of the Colloidal CdS−ZnO System. *J. Phys. Chem.* **1992**, *96*, 6834−6839.

(58) Song, X.; Yu, X.-L.; Xie, Y.; Sun, J.; Ling, T.; Du, X.-W. Improving Charge Separation of Solar Cells by the Co-sensitization of CdS Quantum Dots and Dye. *Semicond. Sci. Technol.* **2010**, *25*, 095014.

(59) Markov, D. E.; Tanase, C.; Blom, P. W. M.; Wildeman, J. Simultaneous Enhancement of Charge Transport and Exciton Diffusion in Poly(*p*-phenylene vinylene) Derivatives. *Phys. Rev. B* **2005**, *72*, 045217.

(60) Lewis, A. J.; Ruseckas, A.; Gaudin, O. P. M.; Webster, G. R.; Burn, P. L.; Samuel, I. D. W. Singlet Exciton Diffusion in MEH-PPV Films Studied by Exciton−Exciton Annihilation. *Org. Electron.* **2006**, *7*, 452−456.

(61) Hwang, I.; Scholes, G. D. Electronic Energy Transfer and Quantum-Coherence in π-Conjugated Polymers. *Chem. Mater.* **2011**, *23*, 610−620.

(62) The effects of the CdS layer (e.g., *L* = 3−8 nm) over ITO substrate on the light intensity into MEH-PPV between nanorods is ignorable, because only ca. 1% of incident light intensity is attenuated when passing through a CdS layer with a thickness of 10 nm according to the relation $I = I_0 \exp(-\alpha x)$, where I_0 is the incident intensity, x is the illumination depth (i.e., $x = L$), and $\alpha = 10^4$ cm^{-1} is the absorption coefficient of CdS.

(63) Raut, B. T.; Godse, P. R.; Pawar, S. G.; Chougule, M. A.; Patil, V. B. Development of Nanostructured CdS Sensor for H$_2$S Recognition: Structural and Physical Characterization. *J. Mater. Sci.: Mater. Electron.* **2012**, *23*, 956−963.

(64) Quintana, M.; Edvinsson, T.; Hagfeldt, A.; Boschloo, G. Comparison of Dye-Sensitized ZnO and TiO$_2$ Solar Cells: Studies of Charge Transport and Carrier Lifetime. *J. Phys. Chem. C* **2007**, *111*, 1035−1041.

(65) de Jongh, P. E.; Vanmaekelbergh, D. Trap-Limited Electronic Transport in Assemblies of Nanometer-Size TiO$_2$ Particles. *Phys. Rev. Lett.* **1996**, *77*, 3427−3430.

(66) Vanmaekelbergh, D.; de Jongh, P. E. Electron Transport in Disordered Semiconductors Studied by a Small Harmonic Modulation of the Steady State. *Phys. Rev. B* **2000**, *61*, 4699−4704.

(67) Haque, S. A.; Tachibana, Y.; Klug, D. R.; Durrant, J. R. Charge Recombination Kinetics in Dye-Sensitized Nanocrystalline Titanium Dioxide Films under Externally Applied Bias. *J. Phys. Chem. B* **1998**, *102*, 1745−1749.

(68) Bisquert, J.; Zaban, A.; Salvador, P. Analysis of the Mechanisms of Electron Recombination in Nanoporous TiO$_2$ Dye-Sensitized Solar Cells. Nonequilibrium Steady-State Statistics and Interfacial Electron Transfer via Surface States. *J. Phys. Chem. B* **2002**, *106*, 8774−8782.

(69) Moliton, A.; Nunzi, J.-M. How to Model the Behaviour of Organic Photovoltaic Cells. *Polym. Int.* **2006**, *55*, 583−600.

(70) Marsh, R. A.; McNeill, C. R.; Abrusci, A.; Campbell, A. R.; Friend, R. H. A Unified Description of Current−Voltage Characteristics in Organic and Hybrid Photovoltaics under Low Light Intensity. *Nano Lett.* **2008**, *8*, 1393−1398.

(71) Kawatsu, T.; Coropceanu, V.; Ye, A.; Brédas, J.-L. Quantum-Chemical Approach to Electronic Coupling: Application to Charge Separation and Charge Recombination Pathways in a Model Molecular Donor-Acceptor System for Organic Solar Cells. *J. Phys. Chem. C* **2008**, *112*, 3429−3433.

(72) Kippelen, B.; Brédas, J.-L. Organic Photovoltaics. *Energy Environ. Sci.* **2009**, *2*, 251−261.

(73) Zhu, X.-Y.; Yang, Q.; Muntwiler, M. Charge-Transfer Excitons at Organic Semiconductor Surfaces and Interfaces. *Acc. Chem. Res.* **2009**, *42*, 1779−1787.

(74) Peumans, P.; Forrest, S. R. Separation of Geminate Charge-Pairs at Donor−Acceptor Interfaces in Disordered Solids. *Chem. Phys. Lett.* **2004**, *398*, 27−31.

(75) Morteani, A. C.; Sreearunothai, P.; Herz, L. M.; Friend, R. H.; Silva, C. Exciton Regeneration at Polymeric Semiconductor Hetero-junctions. *Phys. Rev. Lett.* **2004**, *92*, 247402.

(76) Xu, F.; Volkov, V.; Zhu, Y.; Bai, H.; Rea, A.; Valappil, N. V.; Su, W.; Gao, X.; Kuskovsky, I. L.; Matsui, H. Long Electron−Hole Separation of ZnO-CdS Core−Shell Quantum Dots. *J. Phys. Chem. C* **2009**, *113*, 19419−19423.

(77) Wu, S.; Li, J.; Lo, S.-C.; Tai, Q.; Yan, F. Enhanced Performance of Hybrid Solar Cells Based on Ordered Electrospun ZnO Nanofibers Modified with CdS on the Surface. *Org. Electron.* **2012**, *13*, 1569−1575.

(78) Scharber, M. C.; Mühlbacher, D.; Koppe, M.; Denk, P.; Waldauf, C.; Heeger, A. J.; Brabec, C. J. Design Rules for Donors in Bulk-Heterojunction Solar Cells−Towards 10% Energy-Conversion Efficiency. *Adv. Mater.* **2006**, *18*, 789−794.

(79) Olson, C.; Shaheen, S. E.; White, M. S.; Mitchell, W. J.; van Hest, M. F. A. M.; Collins, R. T.; Ginley, D. S. Band-Offset Engineering for Enhanced Open-Circuit Voltage in Polymer−Oxide Hybrid Solar Cells. *Adv. Funct. Mater.* **2007**, *17*, 264−269.

(80) Koster, L. J. A.; Mihailetchi, V. D.; Ramaker, R.; Blom, P. W. M. Light Intensity Dependence of Open-Circuit Voltage of Polymer:-Fullerene Solar Cells. *Appl. Phys. Lett.* **2005**, *86*, 123509.

(81) Rauh, D.; Wagenpfahl, A.; Deibel, C.; Dyakonov, V. Relation of Open Circuit Voltage to Charge Carrier Density in Organic Bulk Heterojunction Solar Cells. *Appl. Phys. Lett.* **2011**, *98*, 133301.

(82) Bisquert, J.; Garcia-Belmonte, G. On Voltage, Photovoltage, and Photocurrent in Bulk Heterojunction Organic Solar Cells. *J. Phys. Chem. Lett.* **2011**, *2*, 1950−1964.

(83) Lee, M. M.; Teuscher, J.; Miyasaka, T.; Murakami, T. N.; Snaith, H. J. Efficient Hybrid Solar Cells Based on Meso-Superstructured Organometal Halide Perovskites. *Science* **2012**, *338*, 643−647.

(84) Usui, H. Influence of Surfactant Micelles on Morphology and Photoluminescence of Zinc Oxide Nanorods Prepared by One-Step Chemical Synthesis in Aqueous Solution. *J. Phys. Chem. C* **2007**, *111*, 9060−9065.

(85) Schwarzburg, K.; Wiliig, F. Influence of Trap Filling on Photocurrent Transients in Polycrystalline TiO_2. *Appl. Phys. Lett.* **1991**, *58*, 2520−2522.

(86) Boschloo, G.; Hagfeldt, A. Activation Energy of Electron Transport in Dye-Sensitized TiO_2 Solar Cells. *J. Phys. Chem. B* **2005**, *109*, 12093−12098.

(87) Cardoso, J. C.; Grimes, C. A.; Feng, X.; Zhang, X.; Komarneni, S.; Zanoni, M. V. B.; Bao, N. Fabrication of Coaxial TiO_2/Sb_2S_3 Nanowire Hybrids for Efficient Nanostructured Organic−Inorganic Thin Film Photovoltaics. *Chem. Commun.* **2012**, *48*, 2818−2820.

(88) Potscavage, W. J., Jr.; Yoo, S.; Kippelen, B. Origin of the Open-Circuit Voltage in Multilayer Heterojunction Organic Solar Cells. *Appl. Phys. Lett.* **2008**, *93*, 193308.

(89) Potscavage, W. J., Jr.; Sharma, A.; Kippelen, B. Critical Interfaces in Organic Solar Cells and Their Influence on the Open-Circuit Voltage. *Acc. Chem. Res.* **2009**, *42*, 1758−1767.

(90) Vandewal, K.; Tvingstedt, K.; Gadisa, A.; Inganäs, O.; Manca, J. V. Relating the Open-Circuit Voltage to Interface Molecular Properties of Donor:Acceptor Bulk Heterojunction Solar Cells. *Phys. Rev. B* **2010**, *81*, 125204.

(91) Guijarro, N.; Lana-Villarreal, T.; Shen, Q.; Toyoda, T.; Gómez, R. Sensitization of Titanium Dioxide Photoanodes with Cadmium Selenide Quantum Dots Prepared by SILAR: Photoelectrochemical and Carrier Dynamics Studies. *J. Phys. Chem. C* **2010**, *114*, 21928−21937.

(92) Žídek, K.; Zheng, K.; Ponseca, C. S., Jr.; Messing, M. E.; Wallenberg, L. R.; Chábera, P.; Abdellah, M.; Sundström, V.; Pullerits, T. Electron Transfer in Quantum-Dot-Sensitized ZnO Nanowires: Ultrafast Time-Resolved Absorption and Terahertz Study. *J. Am. Chem. Soc.* **2012**, *134*, 12110−12117.

(93) Bouclé, J.; Chyla, S.; Shaffer, M. S. P.; Durrant, J. R.; Bradley, D. D. C.; Nelson, J. Hybrid Solar Cells from a Blend of Poly(3-hexylthiophene) and Ligand-Capped TiO_2 Nanorods. *Adv. Funct. Mater.* **2008**, *18*, 622−633.

(94) Tai, Q.; Zhao, X.; Yan, F. Hybrid Solar Cells Based on Poly(3-hexylthiophene) and Electrospun TiO_2 Nanofibers with Effective Interface Modification. *J. Mater. Chem.* **2010**, *20*, 7366−7371.

(95) Snaith, H. J.; Moule, A. J.; Klein, C.; Meerholz, K.; Friend, R. H.; Grätzel, M. Efficiency Enhancements in Solid-State Hybrid Solar Cells via Reduced Charge Recombination and Increased Light Capture. *Nano Lett.* **2007**, *7*, 3372−3376.

5637

dx.doi.org/10.1021/jp312728t | *J. Phys. Chem. C* 2013, 117, 5626−5637